# Chapter 6

## Ti-Nb-Ta-$Fe_{0.35}$-$Co_{0.35}$ nanocrystalline HEA

### 6.1. Introduction

Metallic biomaterials have gained immense interest as prosthetics for damaged hard tissues such as dental roots, knee and hip joints, etc. [264, 265]. However, commonly employed conventional metallic implant materials such as 316L stainless steel (SS), Co-Cr-Mo alloy, commercially pure titanium (cp-Ti), and Ti-alloys surpass human bone's elastic modulus, causing stress shielding and potential complications such as bone cell death, implant loosening, or implant failure [266, 267]. Further, the cytotoxic concerns due to Al and V compel its wide acceptance [268]. These toxic atoms can inhibit bone growth, thereby leading to peripheral neuropathy and Alzheimer's disease. Therefore, to mitigate the adverse effects associated with existing Ti-based alloys, it is important to explore novel categories of Ti-alloys.

Amongst various Ti-alloys, its BCC alloys have lower hardness values. In contrast to other elements, the smaller-sized Co and Fe readily dissolve into the lattice and thus contribute to solid solution strengthening [269]. In addition, Fe and Co also increase resistance against corrosive environments (both acidic and alkaline), thereby enhancing the durability of the Ti-alloys in such conditions [242]. These elements have even lower melting points than noble elements like W, Hf, Zr, and Mo. The density of Fe and Co is lower than that of alloying elements used for biomaterials such as Hf and Mo. Hence, the incorporation of Fe and Co into HEAs may offer a feasible approach to enhance their biocompatibility at lower expenses.

Based on these research findings, we propose a novel class of HEA consisting of elements like Ti, Nb, Ta, Co, and Fe. This formulation can produce HEA with enhanced hardness, and improved biocompatibility. After reviewing the existing literature, it has been observed that this particular combination of HEA has yet to be explored as a potential implant material.

In this chapter, the synthesis of nanocrystalline Ti-Nb-Ta-$Fe_{0.35}$-$Co_{0.35}$ HEA using MA followed by SPS at 1000 °C is reported. For, the alloyed powder and SPSed sample, phase evolution, microstructure, and phase stability were analyzed using XRD, TEM, SEM, and DSC. The mechanical and physical properties (i.e., density, porosity, hardness, Young's modulus, and compressive strength) of the consolidated sample were also examined. Cell culture analysis was carried out to assess the biocompatibility of the sintered sample using MG-63 cells.

## 6.2. Experimental summary

Ti-Nb-Ta-$Fe_{0.35}$-$Co_{0.35}$ HEA has been synthesized by MA, followed by SPS at 1000 °C. The method of preparation, microstructural characterization, mechanical, and in-vitro assessment techniques have been outlined in Chapter 3.

## 6.3. Results and discussion

### *6.3.1 Alloy Design*

In this study, the design of the HEAs system is based on the parametric approach. This approach is characterized by the incorporation of empirical alloy parameters, such as mixing enthalpy ($\Delta H_{mix}$), mixing entropy ($\Delta S_{mix}$), atomic radii difference ($\delta$), and a dimensionless parameter ($\Omega$). The contribution of mixing entropy is the prime concern for the formation of any HEA. This phenomenon is elucidated in Eq. (2.1), highlighting the relevance of the interplay between thermodynamic factors in HEA formation. The increase in mixing entropy

decreases the free energy, thereby reducing the tendency of being ordered. The fundamental parameters governing solid solution formation are defined in Eqs. (2.2-2.4). These equations capture the key factors contributing to the stability and formation of solid solutions in HEAs.

The values of mixing enthalpy $\Delta H_{i-j}$ for possible binary alloys in the Ti-Nb-Ta-Fe-Co HEA system are presented in Table 6.1. From Table 6.1, it is evident that the binary mixing enthalpy ($\Delta H_{mix}^{AB}$) for the selected HEA exhibits both positive and negative values. Moreover, a higher absolute value of mixing enthalpy can also hinder the solid solutions formation in HEAs; ideally it should fall in the range of $-22 \leq \Delta H_{mix} \leq 7$ kJ/mol. The binary mixing enthalpy of Co-Ti (-28), Co-Nb (-25), Co-Ta (-24), Fe-Ti (-17), Fe-Nb (-16), and Fe-Ta (-15) reveals higher negative values. These higher negative values suggest that adding Fe and Co into Ti-Nb-Ta alloys impedes the formation of a solid solution. However, the addition of Co and Fe in Ti-Nb-Ta alloys significantly enhances $\Delta S_{mix}$, positively impacting the mixing entropy. Table 6.2 represents the binary atomic size differences (%) between the elements in the Ti-Nb-Ta-Fe-Co alloy system. A negligible difference in the atomic size between Fe and Co can be observed in Table 6.2. Fe and Co possess smaller atomic sizes than other elements (e.g. Ti, Nb, and Ta), allowing them to easily dissolve into the lattice of the alloys. Further, the incorporation of Fe and Co could provide significant solid solution strengthening [243]. Numerous studies have explored the possibility of developing bio-HEAs by incorporating elements such as Ti, Sn, Cr, Nb, Zr, Hf, Mo, Mn, and Ta [270, 271]. Previous studies have also suggested that Ti having Fe and Co possess better mechanical properties and exhibit favourable biocompatibility, thus can be used as a potential implant material [8, 272]. Thus, integrating Fe and Co in optimized concentrations into the Ti-Nb-Ta alloy system helps in attaining desirable properties required for implant applications. Consequently, this research synthesized and analyzed 5-component Ti-Nb-Ta-$Fe_x$-$Co_x$ ($x > 0$) alloys.

Figure 6.1 illustrates the governing empirical alloy parameters for predicting the solid solution formation in the Ti-Nb-Ta-$Fe_x$-$Co_x$ alloy system. The variation of $\triangle S_{mix}/R$ with increasing values of x is shown in Fig. 6.1(a). As the value of x increases, the $\triangle S_{mix}/R$ ratio also increases. Consequently, to ensure $\triangle S_{mix}/R \geq 1.5$, the minimum value of x is determined to be 0.35. In Fig. 6.1(b), the values of $\triangle H_{mix}$ for the Ti-Nb-Ta-$Fe_x$-$Co_x$ HEA are presented. These values are negative, and their absolute magnitude progressively increases with x values. This suggests that, when considering the interactions between the constituent elements, the formation of a solid solution is not favoured with higher concentrations of Fe and Co (i.e., larger x values). Table 6.3 shows that Fe and Co possess significantly smaller atomic radii than Ti, Nb, and Ta. This disparity in atomic radii contributes to an increase in the δ value with the increase in the concentration of Fe and Co, i.e. a higher value of x (Fig. 6.1c). Therefore, to achieve favourable values of $\triangle H_{mix}$ and δ for forming this HEA, it is advisable to keep the value of x as low as possible. By minimizing x, the formation of intermetallic compounds can also be prevented, and thus, the desired properties of the alloy will be achieved. For the present HEA, the computed value of δ where x has the minimum possible value satisfying the relation $\triangle S_{mix}/R \geq 1.5$ is determined to be 5.5. The variation of parameter Ω with increasing values of x is depicted in Fig. 6.1(d), revealing a decrease in Ω values. The value of Ω greater than 1.1 favours the solid solution formation. The computed thermodynamic parameters for the Ti-Nb-Ta-$Fe_{0.35}$-$Co_{0.35}$ HEA system are presented in Table 6.4. Based on its VEC $<$ 6.87 and $\Omega >$ 1.1, it is predicted that the crystal structure of this HEA system should be BCC.

**Table 6.1** Binary mixing enthalpy ($\Delta H_{ij}^{mix}$, kJ/mol) following Miedema's approach for Ti-Nb-Ta-Fe-Co HEA [222]

| Elements | Ti | Nb | Ta | Fe | Co |
|---|---|---|---|---|---|
| Ti | - | 2 | 1 | -17 | -28 |
| Nb | 2 | - | 0 | -16 | -25 |
| Ta | 1 | 0 | - | -15 | -24 |
| Fe | -17 | -16 | -15 | - | -1 |
| Co | -28 | -25 | -24 | -1 | - |

**Table 6.2** Values of binary atomic size differences (δ, %) in Ti-Nb-Ta-Fe-Co HEA

| Elements | Ti | Nb | Ta | Fe | Co |
|---|---|---|---|---|---|
| Ti | - | 1.1 | 1.1 | 8.2 | 7.7 |
| Nb | 1.1 | - | 0.03 | 7.0 | 6.6 |
| Ta | 1.1 | 0.03 | - | 7.1 | 6.6 |
| Fe | 8.2 | 7.0 | 7.1 | - | 0.4 |
| Co | 7.7 | 6.6 | 6.6 | 0.4 | - |

**Table 6.3** Physiochemical properties of elements in Ti-Nb-Ta-Fe-Co HEA

| Elements | Ti | Nb | Ta | Fe | Co |
|---|---|---|---|---|---|
| Atomic radius (Å) | 1.462 | 1.429 | 1.430 | 1.241 | 1.251 |
| Melting point ($^0$C) | 1668 | 2477 | 3017 | 1538 | 1495 |
| Crystal structure | HCP | BCC | BCC | BCC | HCP |
| VEC | 4 | 5 | 5 | 8 | 9 |
| Young's modulus (GPa) | 116 | 105 | 186 | 211 | 209 |
| Density (g.cm$^{-3}$) | 4.50 | 8.57 | 16.69 | 7.87 | 8.90 |

**Table 6.4** Computed thermodynamical parameters of Ti-Nb-Ta-$Fe_{0.35}$-$Co_{0.35}$ HEA

| $\triangle S_{conf.}$ ($JK^{-1}mol^{-1}$) | δ (%) | $\triangle H_{mix}$ ($kJ.mol^{-1}$) | $T_m$ (°C) | Ω | VEC |
|---|---|---|---|---|---|
| 12.5 | 5.5 | -11.9 | 2222.5 | 2.6 | 5.4 |

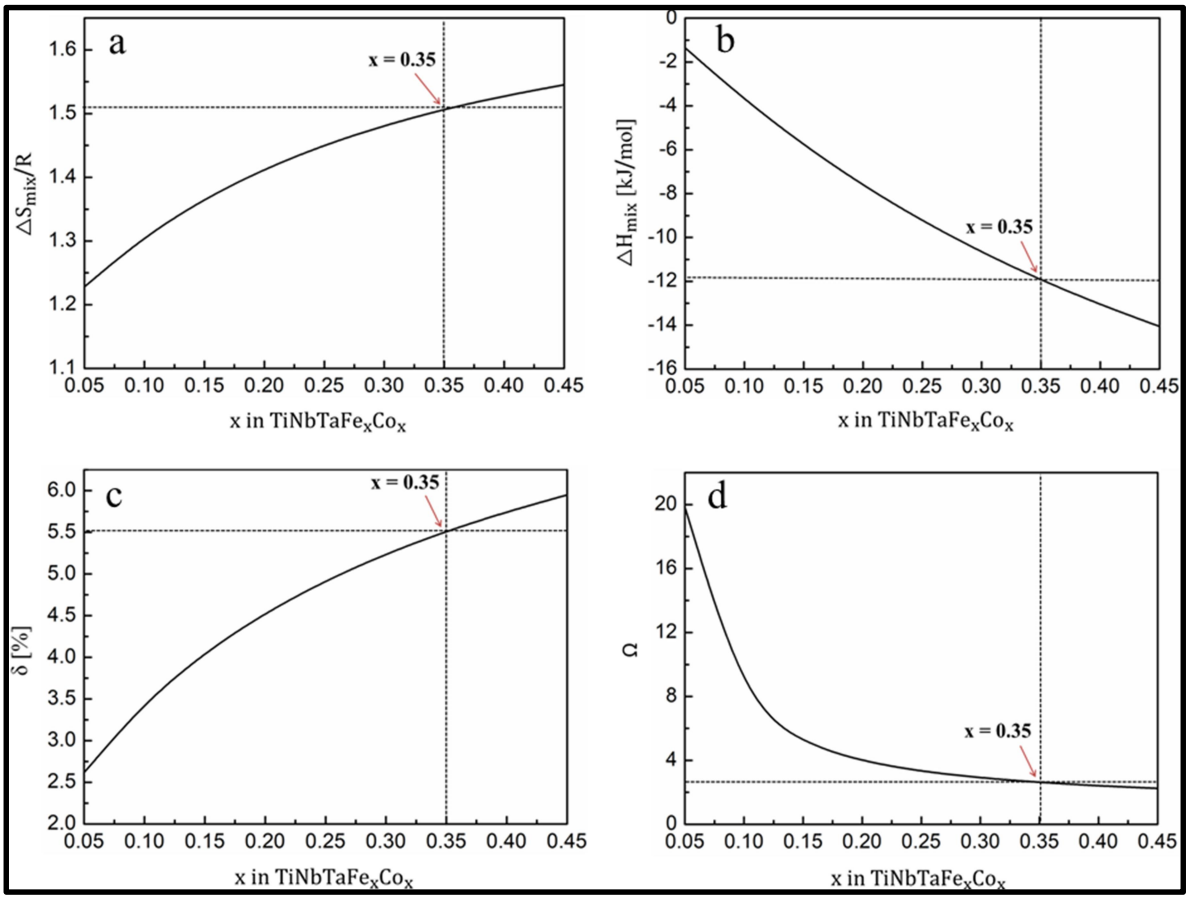


**Fig. 6.1.** Empirical alloy parameters to predict the possible formation of a solid solution in Ti-Nb-Ta-$Fe_x$-$Co_x$ HEA, (a) $\triangle S_{mix}/R$, (b) $\triangle H_{mix}$ ($kJ.mol^{-1}$), (c) δ (%), and (d) Ω.

*6.3.2 Synthesis of nanocrystalline HEA powder by MA*

Figure 6.2 illustrates the XRD patterns of the milled Ti-Nb-Ta-$Fe_{0.35}$-$Co_{0.35}$HEA powder obtained after different milling durations. Initially, during the early stages of MA (i.e., after 10 min), the diffraction peaks associated with each element are prominently observed. However, with the progression of milling, the relative intensities of elemental peaks gradually

diminish. Additionally, the diffraction patterns show peak broadening with increased milling durations. This can be attributed to two primary factors: high lattice strain and reduced crystallite size resulting from milling [140, 247]. After 5 h of MA, the minor peaks corresponding to Ti, Fe, and Co disappeared, while the major peaks exhibited decreased intensity and increased broadness. This suggests a stage for the initiation of solid solution formation [140]. With an extended milling duration of upto 20 h, the Ti peak (d ~ 2.798 Å (101) disappears, accompanied by an increase in the peak broadness and a decrease in the intensities of the remaining peaks. After 40 h of MA, most peaks lost their identity and were accommodated in the BCC solid solution. The Nb-Ti, Ti-Ta, and Nb-Ta phase diagrams suggest that these elements have mutual solubility [249]. Further, the BCC structure of Nb, Ta, and Fe might have dominated which leads to the formation of BCC-structured HEA. The milling duration was extended for 50 h to observe any further changes induced by the milling process. This extended milling duration further facilitates the complete dissolution of the alloying elements and forming a more homogenized HEA. After 50 h of MA, the HEA powder consisted of a single-phase BCC structure. For this sample, the precision lattice parameter was found to be (3.305 $\pm$ 0.007 Å). This value closely aligns with the lattice parameters of BCC Ti, Nb, and Ta (3.311, 3.306, and 3.305 Å). Hence, these three elements might have formed the host lattice for the current HEA.

The XRD peak profile is subjected to analysis using the pseudo-Voigt function to calculate the lattice strain (LS) and crystallite size (CS) of the milled samples. The instrumental broadening contribution of the reference sample silicon is eliminated. The analysis follows the Williamson-Hall method, and the relationship between CS and LS is expressed in Eq. (4.1).

Figure 6.3 illustrates the distribution patterns for the CS (nm) and LS (%) of the alloyed HEA powder for different milling periods. It can be observed that LS increases and CS decreases with the increased duration of MA. There is a significant drop in CS during the early milling stage, revealing that most size reduction occurs during the initial hours of MA. As milling progresses, the CS continues to reduce but at a decreasing rate until it reaches a saturation point. This reduction in CS can be ascribed to the impacts of mechanical milling. Smaller CS generally results in increased hardness, strength, and improved wear resistance [273]. Moreover, during the early stages of milling, there is a significant increase in lattice strain (LS), which gradually continues to increase at a slower rate during the later milling durations. The enhancement of lattice strain in HEAs is influenced by element size differences, more grain boundaries from crystallite refinement, and higher dislocation density due to plastic deformation during milling [151, 250]. There is a refinement in the CS from ~39 nm (2 h) to ~7 nm and LS from ~0.24 % (2 h) to ~0.98 % after 50 h of milling. These findings confirm the nanocrystalline characteristic of the alloyed HEA powder.

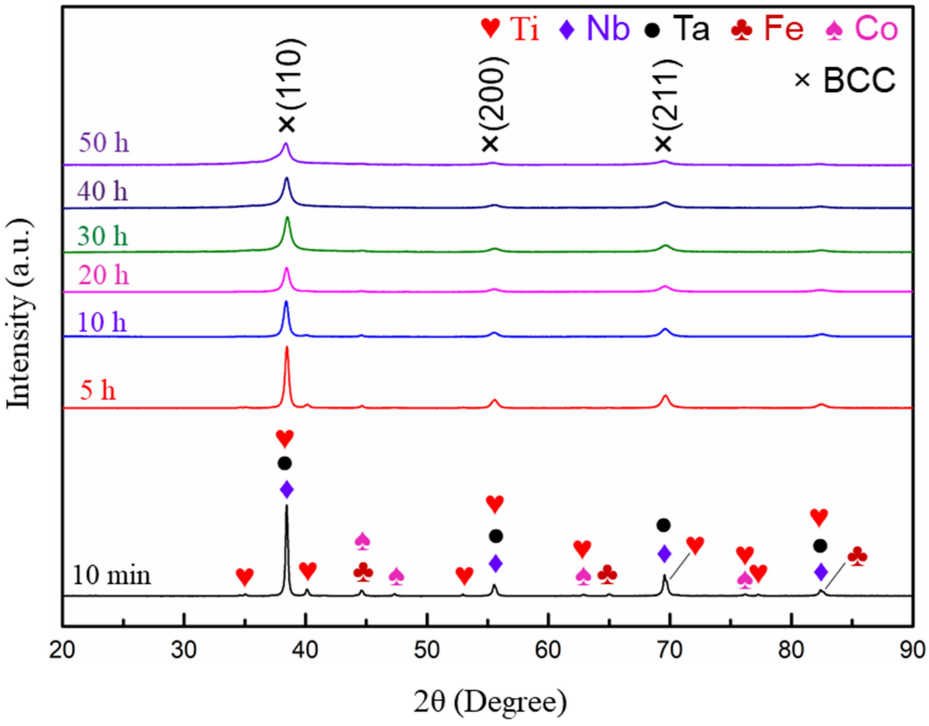


**Fig. 6.2.** XRD patterns of Ti-Nb-Ta- $Fe_{0.35}$ -$Co_{0.35}$ HEA powders at different milling duration.

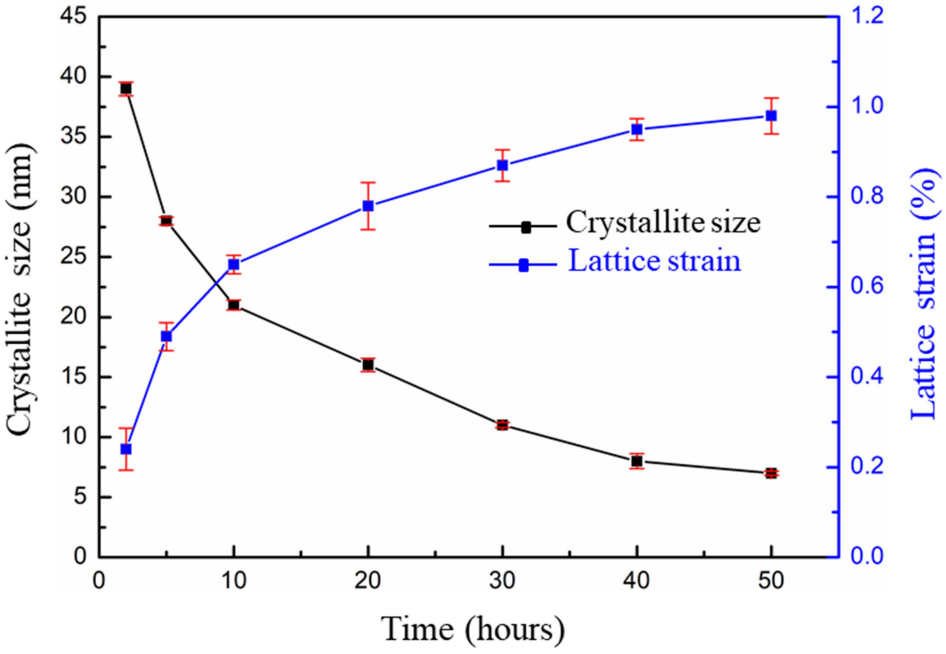


**Fig. 6.3.** Distribution patterns of crystallite size and lattice strain as a function of milling time.

TEM analysis was conducted to investigate the microstructure and crystal structure of the HEA particles obtained after 50 h of MA. The results are presented in Fig. 6.4, including a bright field image and its corresponding SAD pattern. The bright field image (Fig. 6.4a) reveals the presence of irregular dark particles resembling their agglomeration. It was similar to the microstructure obtained after the milling of alloys. The SAD pattern (Fig. 6.4b) confirms the polycrystalline nature of the particles, exhibiting distinct rings corresponding to the (110), (200), and (211) crystallographic planes of a BCC structure. The ring patterns validate the formation of a single-phase solid solution with a lattice parameter of ($a = 3.308 \pm 0.002$ Å). The calculated d-spacing values corresponding to these rings are in agreement with those obtained from the XRD patterns.

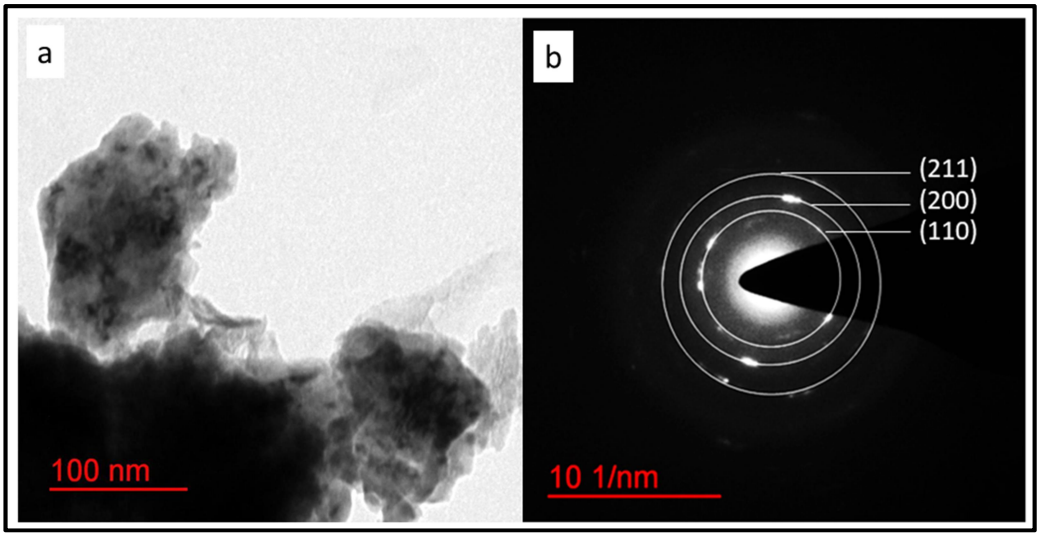


**Fig. 6.4.** TEM images of the Ti-Nb-Ta- $Fe_{0.35}$ -$Co_{0.35}$ HEA powder milled for 50 h, (a) bright field image, and (b) SAD pattern.

To examine the microstructure of the milled Ti-Nb-Ta-$Fe_{0.35}$-$Co_{0.35}$ HEA powder, SEM analysis was conducted. Figure 6.5(a-d) shows the SEM images captured at different milling intervals (10 min, 2 h, 10 h, and 50 h). Studies have reported that the MA process consists of three stages: the early stage, intermediate stage, and completion stage [274, 275]. In the early stage, powder particles are soft, easily flattening into a layered structure with various initial constituents, as depicted in Fig. 6.5(b) after 2 h of MA. The intermediate stage involves a cyclic process of continuous deformation, fracture, and cold welding of the particles. The powders remain soft during this stage, and fracture becomes predominant. Consequently, the powders undergo size reduction compared to the initial stage, and the formation of agglomerates becomes apparent, as depicted in Fig. 6.5(c) after 10 h of milling. Subsequent milling progresses to a steady-state equilibrium, known as the completion stage of MA. During this stage, a balance is established between cold welding and fracture processes. Smaller particles resist deformation more but are prone to welding, resulting in larger particles. Consequently, fine and large particles converge towards an intermediate size, as illustrated in Fig. 6.5(d) after 50 h of MA.

Figure 6.5(e) represents the SEM-EDS study of the 50 h milled powder. The EDS elemental composition of the 50 h milled powder is presented in Table 6.5. The results indicate a close resemblance between the observed and actual chemical composition, suggesting a uniform distribution of all elements. However, minor deviations may be attributed to the inherent limitations in the accuracy of EDS analysis. Figure 6.6 depicts the elemental mapping of the elements present in the 50 h milled powder, revealing a homogeneous distribution of all elements in the HEA. The homogeneity in element distribution is desirable for every application, as it can improve mechanical properties and increase stability.

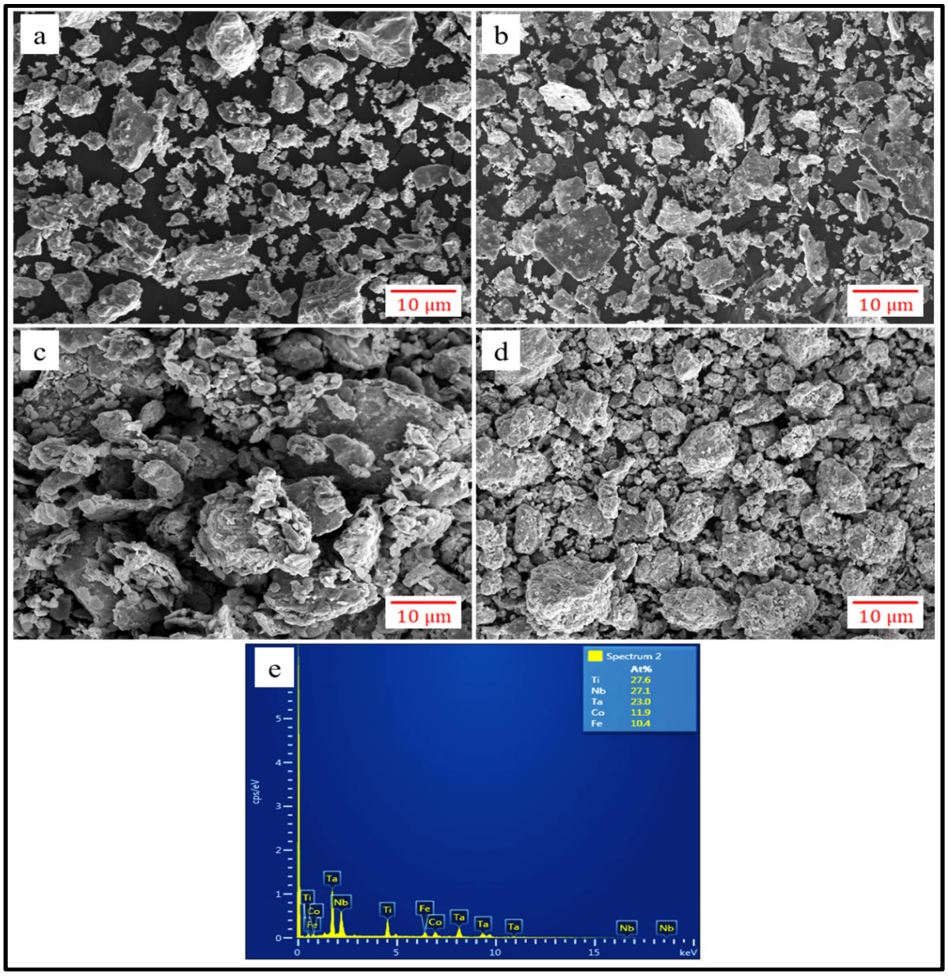


**Fig. 6.5.** SEM morphology of Ti-Nb-Ta-$Fe_{0.35}$-$Co_{0.35}$ HEA powder milled for various intervals, (a) 10 min, (b) 2 h, (c) 10 h, (d) 50 h, and (e) EDS spectrum of 50 h milled powder with composition of alloying elements.

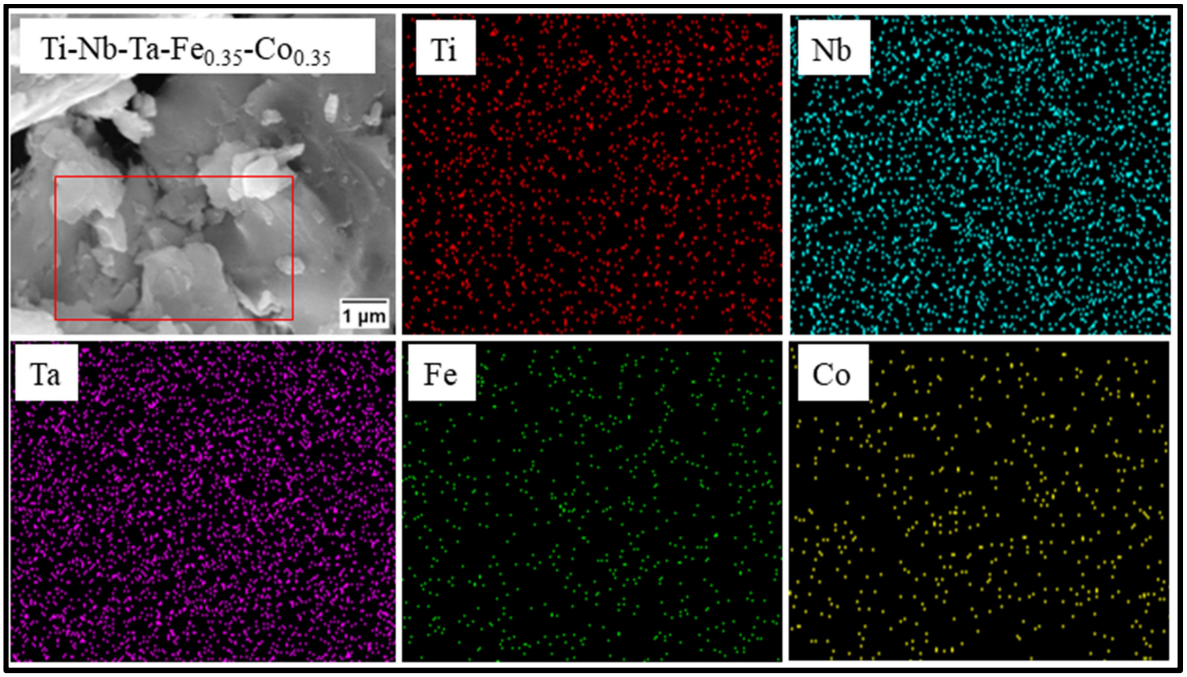


**Fig. 6.6.** SEM-EDS elemental mapping showing the homogeneous elemental distribution in 50 h milled HEA powder.

**Table 6.5** Elemental composition of 50 h alloyed Ti-Nb-Ta-$Fe_{0.35}$-$Co_{0.35}$ HEA sample

| | Elemental composition (at. %) | | | | |
|---|---|---|---|---|---|
| | Ti | Nb | Ta | Fe | Co |
| Actual composition | 27.03 | 27.03 | 27.03 | 9.46 | 9.46 |
| Observed composition | 27.61 | 27.11 | 23.01 | 10.36 | 11.91 |

*6.3.3 Thermal stability of the milled powder, analysis of the phase evolution and microstructure of the sintered sample*

DSC analysis was performed to examine the thermal stability of the milled powder. The DSC thermogram of the 50 h milled powder is presented in Fig. 6.7. The thermogram shows a sharp endothermic peak at around ~812 °C, indicating a phase transformation at this temperature. The phase transformation from BCC to BCC and HCP was confirmed from the

XRD pattern of the sample sintered at 1000 °C, Fig. 6.8. The milled powder consists of elements having high melting temperatures, such as Ta and Nb. Consequently, achieving proper sintering before reaching the transformation temperature becomes challenging. Sintering before the transformation temperature could result in inadequate density and strength. Hence, to promote enhanced sintering with limited grain growth, SPS was conducted at 1000 °C. The XRD peak pattern of the SPSed sample is shown in Fig. 6.8. The diffraction peaks exhibit increased intensity and sharpness compared to the unsintered powder. This enhancement might be attributed to the reduced defects introduced during the MA process, the coarsening of grains, and the release of internal stresses during the solidification [276]. The XRD pattern indicates the coexistence of dual phases, i.e., BCC and HCP. The BCC phase could be indexed at (110), (200), and (211) planes, whereas the HCP phase had planes at (100), (101), (102), (110), and (112) (Fig. 6.8). It can be noticed that the peak intensity of the BCC phase is greater than those of HCP phase, suggesting a higher amount of the former phase. The severe plastic deformation resulting from MA introduces the defects, which are eliminated during the SPS consolidation. The elimination of defects significantly contributes to phase evolution during the SPS process [150]. Thus, the presence of the HCP phase suggests that the heat treatment at 1000 °C results in more stable phases. The CS of the sintered sample is determined using the Williamson-Hall method. The CS for the BCC phase is calculated to be ∼18.2 nm, whereas, for the HCP phase, it is ∼12.7 nm. This value is relatively higher than its powder counterpart (for BCC = ∼7 nm).

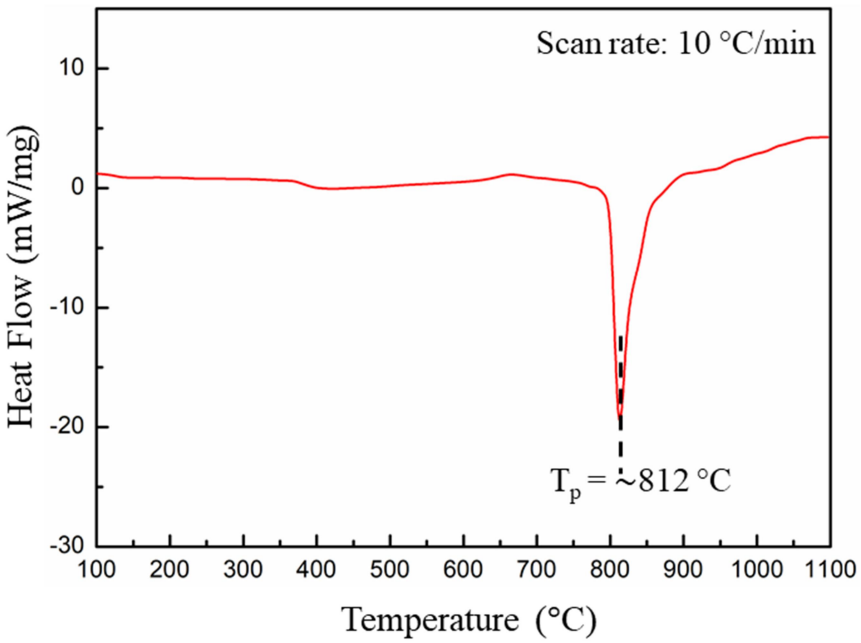


**Fig. 6.7.** DSC thermogram of the 50 h alloyed Ti-Nb-Ta-$Fe_{0.35}$-$Co_{0.35}$ HEA powder.

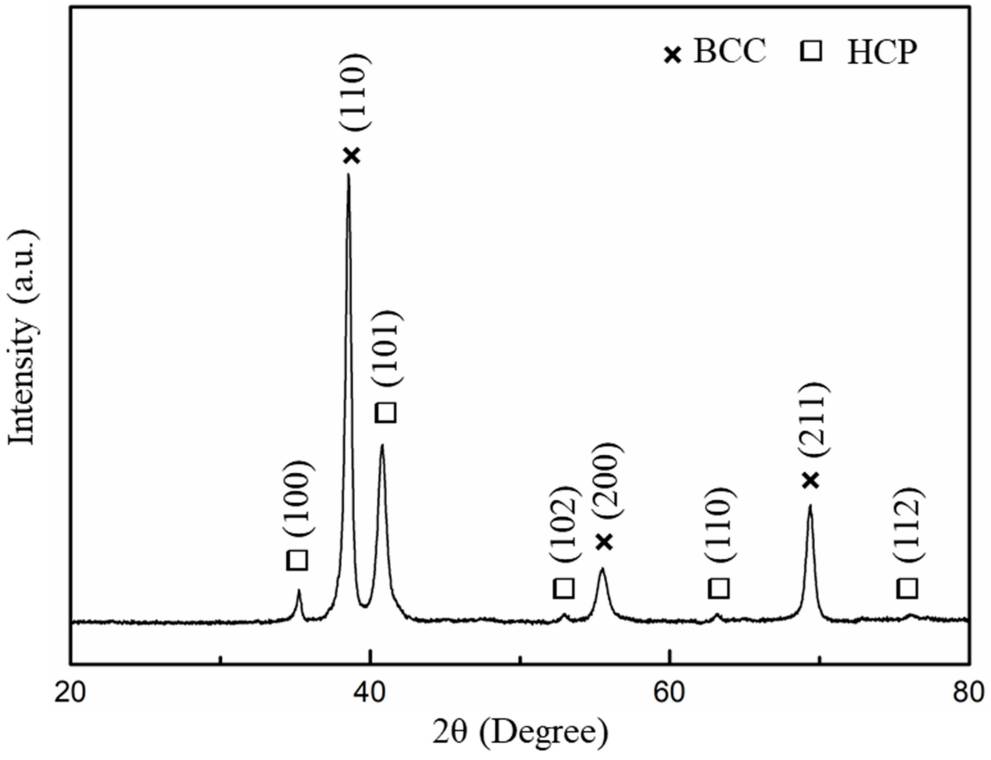


**Fig. 6.8.** XRD pattern of the Ti-Nb-Ta-$Fe_{0.35}$-$Co_{0.35}$ HEA after SPS at 1000 °C.

Figure 6.9(a) reveals the FE-SEM image of the SPSed sample captured in BSE mode. The BSE microstructure reveals the presence of light and dark gray contrast. To substantiate the elemental composition of each contrast region, EDS analysis was conducted. EDS findings indicate that the dark gray contrast region primarily consists of Ti, while the light gray contrast region contains all the alloying elements in significant atomic %. In the BSE microscopic analysis, the light gray region is associated with the BCC phase, whereas the darker region is associated with the HCP phase [224]. The observation of BCC and HCP phases in the BSE microscopy supports and confirms the results obtained from XRD analysis. The preservation of the β (BCC) phase alloy during SPS can be attributed to the combination of short duration and rapid cooling. The introduction of Nb and Ta into the Ti-alloy serves as a β stabilizer, further bolstering its retention and contributing to the desirable properties of the HEA. Figure 6.9(b) shows the selected area EDS for the elements in the SPSed sample, while the corresponding elemental composition is summarized in Table 6.6. The composition of the sintered sample closely matches the nominal composition, signifying the distribution of all elements within the sample. Additionally, Fig. 6.10 showcases the SEM-EDS elemental mapping of the alloying elements present in the SPSed sample. The elemental mapping reveals the distribution of Ti, Nb, Ta, Fe, and Co within the sample (Fig. 6.10). As suggested by the XRD pattern (Fig. 6.8), this material has two phases, which appear as light (BCC) and dark (HCP) in the microstructure shown in Fig. 6.9(a). As the percentage compositions of the elements in the two phases could be uneven and hence elemental mappings were also found to be non-homogeneous.

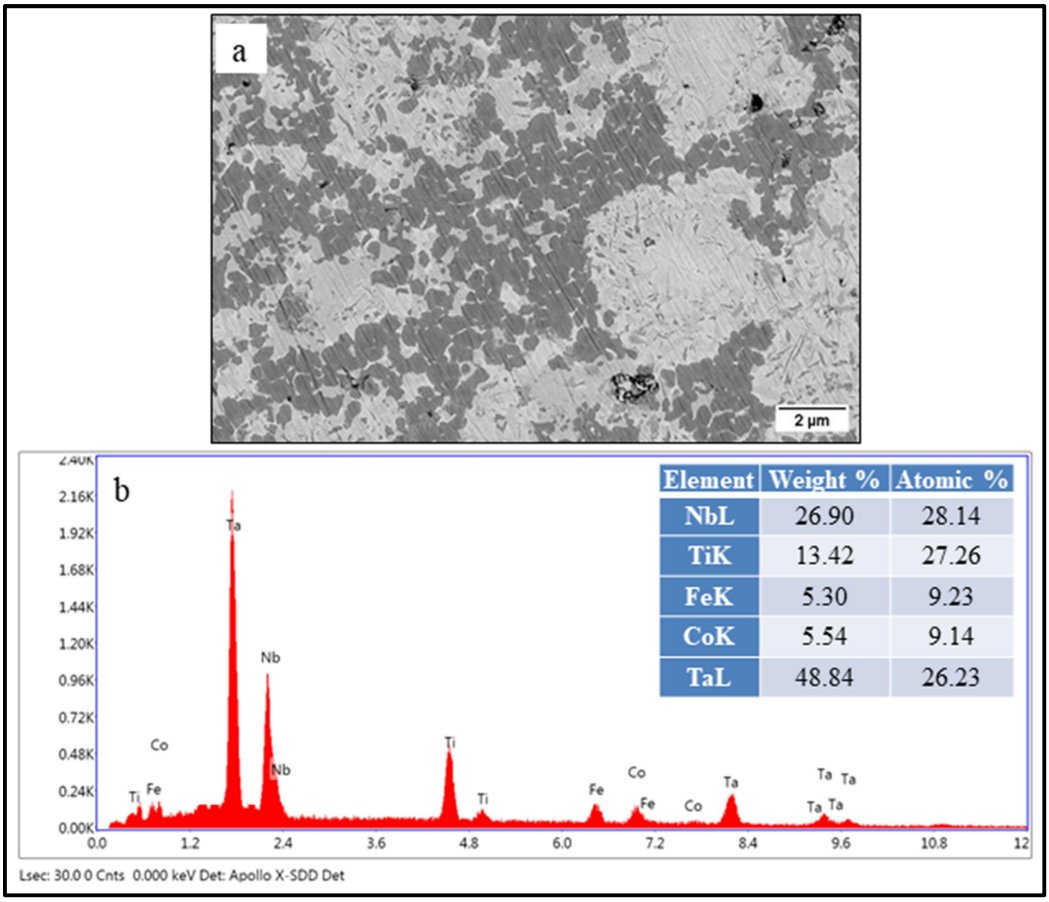


**Fig. 6.9.** FE-SEM image of the sintered sample, (a) backscattered electron mode, and (b) selected area EDS spectrum as well as compositions of the elements.

**Table 6.6** Selected area elemental composition of sintered Ti-Nb-Ta-$Fe_{0.35}$-$Co_{0.35}$ HEA

| Sintered Ti-Nb-Ta-$Fe_{0.35}$-$Co_{0.35}$HEA | Composition (at. %) | | | | |
|---|---|---|---|---|---|
| | Ti | Nb | Ta | Fe | Co |
| Initial composition | 27.03 | 27.03 | 27.03 | 9.46 | 9.46 |
| Final composition | 27.26 | 28.14 | 26.23 | 9.23 | 9.14 |

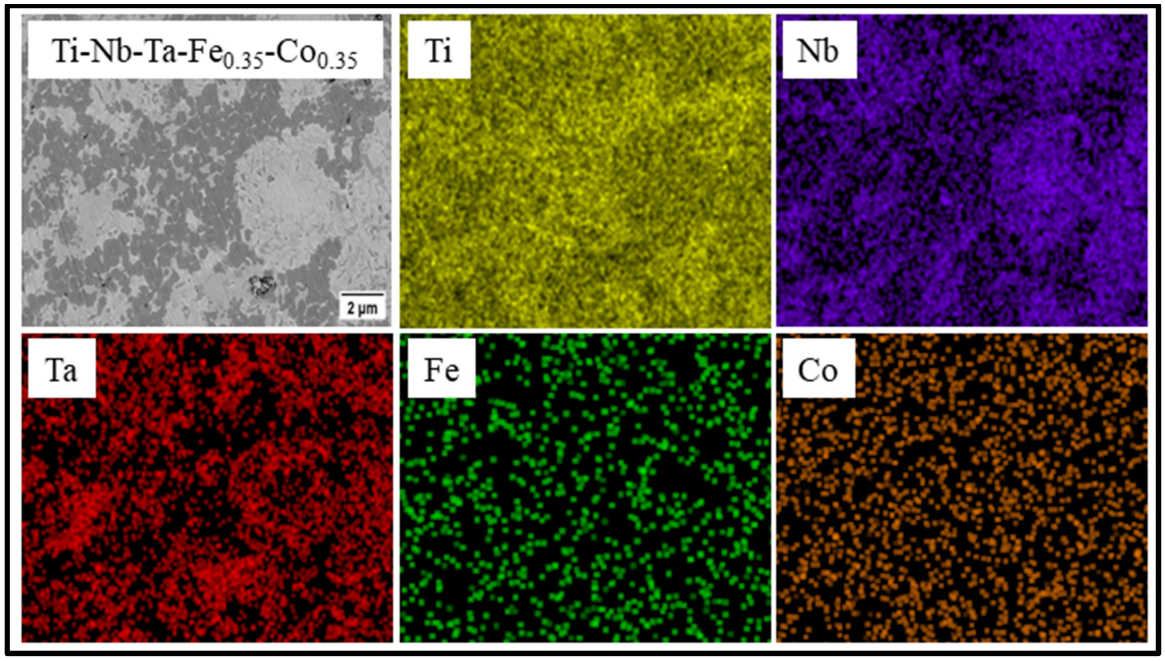


**Fig. 6.10.** SEM-EDS mapping of sintered Ti-Nb-Ta-Cr-$Co_{0.2}$ HEA, showing elemental distribution.

*6.3.4 Physical and mechanical characterization of the sintered sample*

The theoretical density and the porosity within the sample are assessed using the relation given in Eqs. (3.1 and 3.3). The density of the individual element is reported in Table 6.3. For the current HEA, theoretical and the sintered density are calculated as 9.73 g $cm^{-3}$ and 9.45 $\pm$ 0.06 g $cm^{-3}$, respectively. The SPSed sample shows a high relative density of 97.12 $\pm$ 0.6 %, signifying proper densification. The porosity present in the sample is 2.88 $\pm$ 0.6 %. The reason for obtaining higher relative density at lower temperatures can be attributed to the ionization of the particles by localized sparking during the SPS. This localized sparking induces the melting of titanium oxide films and facilitates the formation of neck junctions between powder particles at reduced temperatures [224]. Additionally, SPS promotes limited grain growth and accelerates the interdiffusion between the atoms, resulting in a homogeneous microstructure.

To assess the prospective applicability of the current HEA for bone-replacement implants, instrumented hardness tests were conducted on the sintered sample. Figure 6.11 illustrates the findings from the instrumented hardness testing machine. Figure 6.11(a) presents the load vs. displacement curve of the indentation, while Fig. 6.11(b) provides an optical depiction of the corresponding indentation. The outcomes of the instrument hardness test in conjunction with mechanical and physical properties are shown in Fig. 6.11(c) using a radar diagram. The average value of depth of indentation, Young's modulus, hardness, and compressive strength were determined experimentally to be 7.61 $\pm$ 0.06 μm, 73 $\pm$ 6 GPa, 5.37 $\pm$ 0.5 GPa, and 1295 $\pm$ 20 MPa, respectively. The current HEA shows a lower Young's modulus value compared to the corresponding commonly used bone implant materials such as 316L, Co-Cr-Mo alloy, cp-Ti, and Ti-6Al-4V. Moreover, β-Ti alloys incorporate Ta and Nb as β-phase stabilizing metals to lower Young's modulus and, thereby effectively reduce the adverse effect of the stress-shielding phenomenon [256]. The remarkable alloy hardness (5.37 $\pm$ 0.5 GPa) can be attributed to three factors: (a) homogeneous composition due to MA, (b) solid solution strengthening induced by strong lattice distortion [60], and (c) the presence of an ultrafine-grained structure, leading to enhanced grain boundary strengthening. The Vickers hardness tester was used to ascertain the bulk hardness of the sintered sample. The average value of the Vickers hardness is 614 $\pm$ 15 HV. It's worth highlighting that this hardness is greater than the commonly used biomaterials such as cp-Ti, Ti-6Al-4V, 316L, and Co-Cr-Mo alloy as mentioned in Table 5.7. The present HEA shows high hardness and low Young's modulus compared to currently used biomaterials, although their elastic modulus is still higher than that of human bone (10-30 GPa).

Figure 6.12 depicts the analysis of engineering stress vs. engineering strain for the sintered sample that underwent compression at room temperature. The compressive test reveals a compression strength of 1295 $\pm$ 20 MPa. This level of strength is significantly higher

compared to currently used implant materials. The compressive strength value reported for Ti-6Al-4V is 1080 MPa [232]. This value is comparatively lesser than the compressive strength exhibited by the current HEA. High compressive strength for the current HEA can be primarily attributed to solid solution strengthening, fine-grained microstructures, and local lattice distortion [277]. In HEAs, atoms with distinct atomic sizes and properties induce localized lattice distortion, resulting in local elastic stress fields surrounding the atoms. These local elastic stress fields act as a barrier to dislocation motion and deformation, enhancing compressive strength [259]. Additionally, fine-grained microstructure obtained from MA hinders the propagation of defects and dislocations, ultimately leading to a substantial increase in strength.

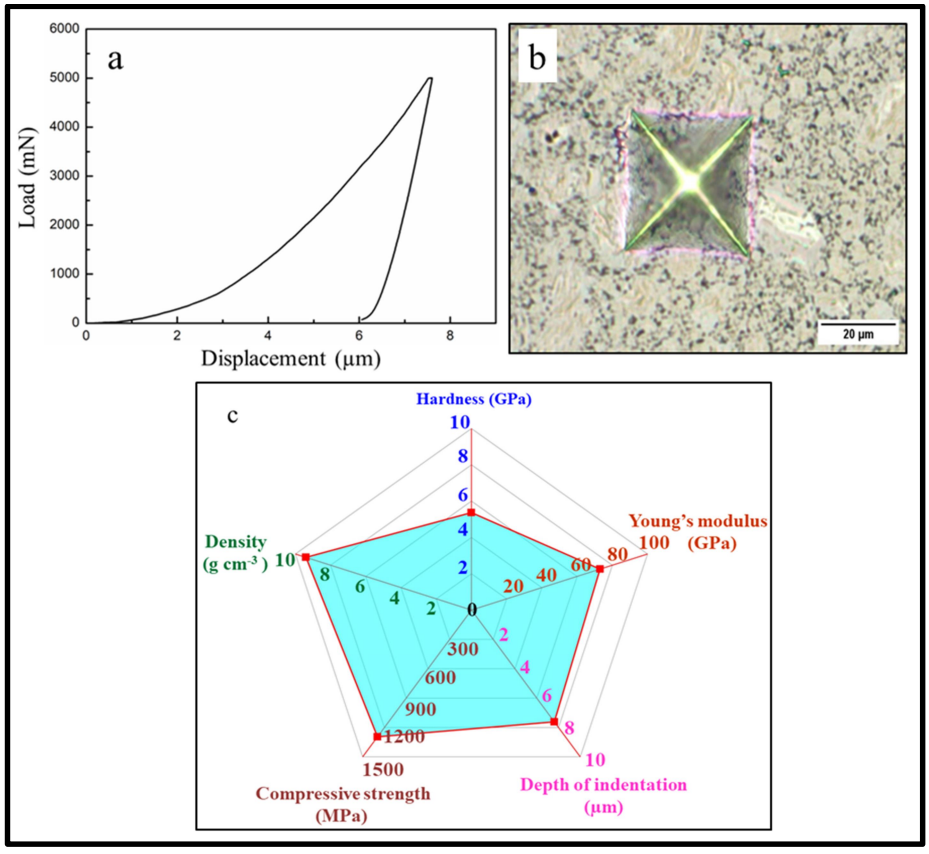


**Fig. 6.11.** (a) Load versus displacement curve obtained from instrument hardness tester, (b) micrograph corresponding to indentation, and (c) Radar diagram showing different mechanical properties.

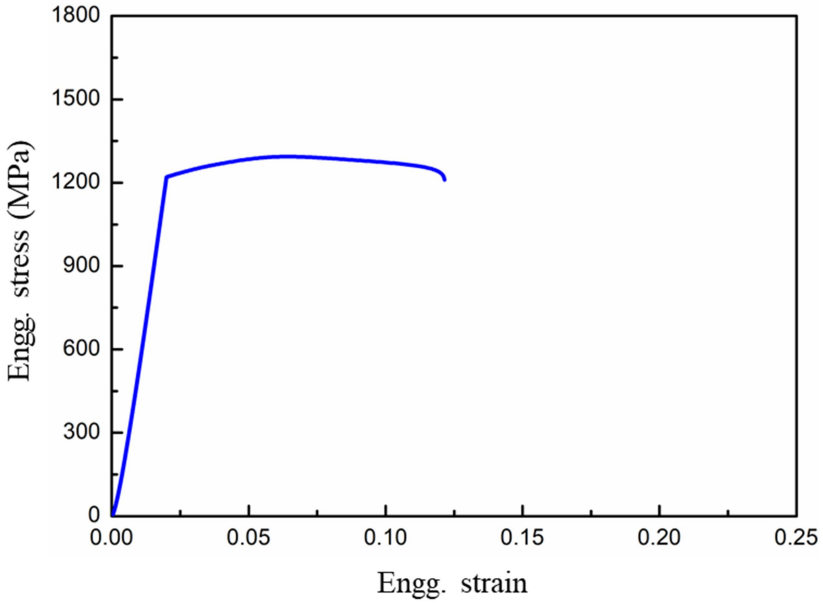


**Fig. 6.12.** Engineering stress-strain curve for a sintered sample under compression at ambient temperature.

*6.3.5 Biocompatibility assessment of the sintered sample*

To assess the suitability of the newly developed implant materials, it is essential to evaluate their interaction with living cells. Hence, biocompatibility of the sintered and cp-Ti samples is conducted using MG-63 cells. Here, cp-Ti, a well-established implant material, has been used as a control sample for comparative analysis. MTT assay was performed over 2, 4, and 6 days to study the cell viability and proliferation of the sintered and cp-Ti samples. Figures 6.13(a) and (b) illustrate the outcomes of cell proliferation and viability assays conducted with MG-63 cells. The optical density (OD) values observed for Ti-Nb-Ta-$Fe_{0.35}$-$Co_{0.35}$ HEA and cp-Ti exhibit a trend of initial increase followed by a subsequent decrease as the incubation period progresses (Fig. 6.13a). Achieving the maximum OD value suggests that the cells have adapted to their surrounding environment over the time [233]. The OD value obtained after 6 days of treatment shows a slight decrease compared to that recorded after 4 days. This decrease is attributed to reduced metabolism due to limited nutrients and

unavailable space. The cell viability % of the sintered alloy was calculated using Eq. (3.8). The cell viability % was measured at different incubation periods, and the results are shown in Fig. 6.13(b). The cell viability % values at different incubation periods were found to be ~92.75 % (2 days), ~97.64 % (4 days), and ~94.31 % (6 days), respectively. As per ISO 10993-5 standard, if cell viability % of the biological material is higher than 75 %, it is considered non-cytotoxic [234]. The MTT assay results reveal that the present HEA has cell viability > 75 % under different incubation periods (2, 4, and 6 days). This suggests its suitability as a potential biomaterial for implant applications without adverse effects on cell growth and metabolic activity**.**

Figure 6.13(c-h) showcases the fluorescence-stained microscopic images illustrating the cultivation of MG-63 cells on the surfaces of the sintered HEA and cp-Ti samples for 2, 4, and 6 days. In the fluorescence-stained micrographs, blue fluorescence depicts the nuclei, while green fluorescence represents the actin cytoskeleton. Following culture periods of different durations (2, 4, and 6 days), the cells cultivated on the sintered HEA and cp-Ti samples show good spreading. This observation strongly implies that both sintered HEA and cp-Ti samples possess significant advantages in promoting the formation of bone matrix [41]. Cells cultured on both samples predominantly exhibited an elongated and spindle-shaped morphology. Cell spreading is crucial for several cellular functions, such as gene expression, cell adhesion, intercellular communication, and cell migration [200].

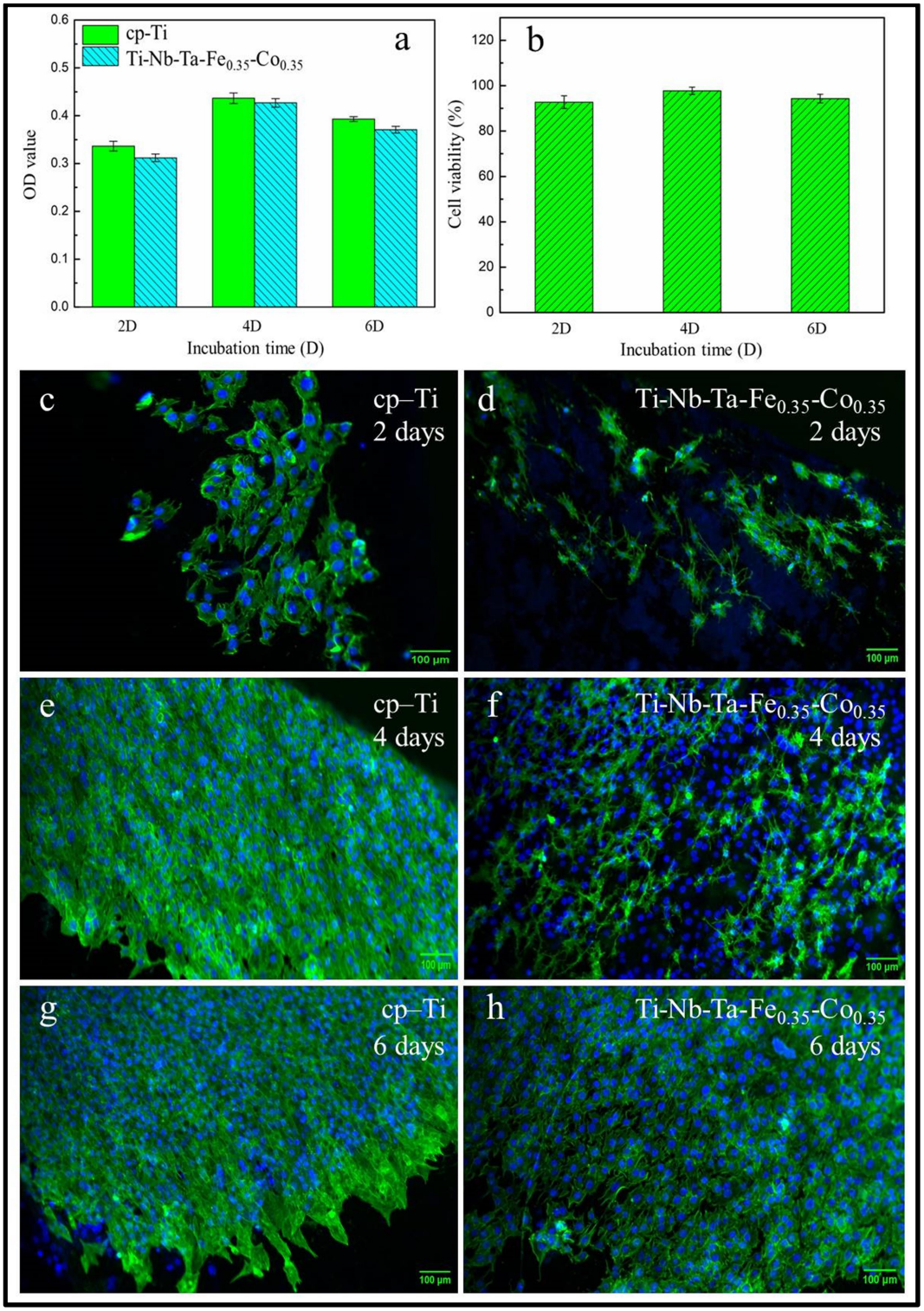


**Fig. 6.13.** MTT assay of the sintered and cp-Ti samples using MG-63 cells cultured on their surfaces after 2, 4, and 6 days of incubation, (a) cell proliferation, and (b) cell viability %. Fluorescence-staining microscopic images of the cells cultured on the surfaces of cp-Ti (c, e, and g) and Ti-Nb-Ta-$Fe_{0.35}$-$Co_{0.35}$ HEA (d, f and h).

## 6.4. Summary

In the present study, Ti-Nb-Ta-$Fe_{0.35}$-$Co_{0.35}$ based HEA was obtained from MA followed by SPS at 1000 °C. The key conclusions obtained from this work can be outlined as follows:

- The semi-empirical thermodynamic parameters (such as $\triangle S_{mix}$, $\delta$, $\triangle H_{mix}$, and $\Omega$) were found within the range for solid solution formation in the current HEA. Furthermore, the calculated VEC value of 5.4 suggests a high probability of its phase to be BCC.
- After 50 h of milling the HEA turned into a monophasic BCC structure (a = 3.305 ± 0.007 Å) which was confirmed from XRD and SAD analysis.
- The DSC thermogram for 50 h milled powder reveals a phase transformation at a temperature of ~812 °C. Hence, after SPS at 1000 °C, the material transformed into BCC and HCP phases.
- For SPSed sample, the mechanical properties, such as Young's modulus, hardness, compressive strength, and were experimentally determined to be ~73 GPa, ~614 HV, and ~1295 MPa, respectively.
- The MTT assay of the sintered sample revealed no toxicity toward MG-63 cells even after 6 days of treatment. Hence, the newly developed Ti-Nb-Ta-$Fe_{0.35}$-$Co_{0.35}$ HEA can be evaluated further as a possible hard tissue replacement material.